

Analysis of the incompressibility constraint in the Smoothed Particle Hydrodynamics method

K. Szewc^{a,*}, J. Pozorski^a, J.-P. Minier^b

^a*Institute of Fluid-Flow Machinery, Polish Academy of Sciences, ul. Fizyka 14, 80-952 Gdańsk, Poland*

^b*Electricité de France, Direction de la Recherche et du Développement, Département Mécanique de Fluides, Energies et Environnement, 6 quai Watier, F-78401 Chatou, France*

Abstract

Smoothed particle hydrodynamics is a particle-based, fully Lagrangian, method for fluid-flow simulations. In this work, fundamental concepts of the method are first briefly recalled. Then, we present a thorough comparison of three different incompressibility treatments in SPH: the weakly compressible approach, where a suitably-chosen equation of state is used; and two truly incompressible methods, where the velocity field projection onto a divergence-free space is performed. A noteworthy aspect of the study is that, in each incompressibility treatment, the same boundary conditions are used (and further developed) which allows a direct comparison to be made. Problems associated with implementation are also discussed and an optimal choice of the computational parameters has been proposed and verified. Numerical results show that the present state-of-the-art truly incompressible method (based on a velocity correction) suffer from density accumulation errors. To address this issue, an algorithm, based on a correction for both particle velocities and positions, is presented. The usefulness of this density correction is examined and demonstrated in the last part of the paper.

Keywords: particle method, SPH, incompressible flows, density correction

1. Introduction

Smoothed Particle Hydrodynamics (SPH) is a fully Lagrangian, particle-based approach for fluid-flow computations. This method was independently proposed by Gingold & Monaghan [1] and Lucy [2] to simulate some astrophysical phenomena at the hydrodynamic level (compressible flow). Nowadays, SPH is more and more often used for flows with interfaces and in geophysical applications. Its main advantage over Eulerian techniques is that there is no requirement of the grid. Therefore, the SPH method is natural to use for complex geometries or multi-phase flows.

An important issue in SPH is the proper implementation of the incompressibility constraints. In the present work, three different implementations are critically discussed and compared for a selection of validation examples. The first one is the Weakly Compressible SPH (WCSPH), which is the most common technique. It involves the standard set of governing equations closed by a suitably-chosen, artificial equation of state, cf. Sect. 4.1. The second and third implementations, called truly incompressible SPH (ISPH), are based on the Projection Method, introduced in SPH by Cummins & Rudman [3]. Generally in ISPH, a Poisson equation is solved to obtain the divergence-free velocity field, cf. Sect. 4.2. In the second approach, this Poisson equation is solved on an auxiliary regular mesh. Here, this method is called the Grid-Projected Poisson Solver (GPPS). Since this approach consists in combining the Eulerian and Lagrangian techniques, it is not an optimal choice for free-surface flows; yet, since SPH has a huge potential in the subject of multi-phase flows, its usefulness seems to be worth of discussion. The third approach considered is the

*Corresponding author: kszewc@imp.gda.pl, tel. +48 58 6995238, fax. +48 58 3416144

ISPH scheme with the Particle Poisson Solver (PPS), cf. Sect. 4.3. In this concept the Poisson equation is rewritten in SPH formulation and solved on the grid of Lagrangian points (particles). The main advantage of this idea is that the additional domain discretization and related discretization errors are avoided. The paper is also related to the work of Lee et al. [4], where a similar comparison between WCSPH and ISPH - PPS approaches has been done. However, in the present work, a comprehensive analysis of boundary conditions is performed. Moreover, since we use the same (ghost-particle) boundary conditions for both WCSPH and ISPH approaches, our comparison offers a new look at the usefulness of the incompressibility variants. For the sake of validation for both single- and two-phase flows, the three different implementations of the incompressibility constraints are compared for the lid-driven cavity flow and the Rayleigh-Taylor instability. For the former case, the impact of various computational parameters on the results have been analyzed and optimal setting has been found; it is consequently used also for the latter case.

A very good comparison of ISPH solvers was presented by Xu et al. [5]. However, the authors do not discuss the problem of accumulating density errors in the ISPH approach. Since, like other authors [3] [6], we have been faced with such a problem, we decided to examine the usefulness of the correction algorithm proposed by Pozorski and Wawreńczuk [7], cf. Sect. 9. This formulation, used also in the PDF computations of turbulent flows [8], consists in retrieving the constant fluid density field by applying the correction to the particles' position. In practice, that procedure involves the computations of the second Poisson solver. The effectiveness of such an approach and the improvement of results are demonstrated.

Another common field of research in SPH is the proper implementation of the boundaries. In the present work, among many techniques, the ghost-particle boundary approach is applied. This implementation involves the use of fictitious external particles that are reflections of the fluid particles in the computational domain. The main advantages of this method are simplicity and conformity with different phases of the fluid [9]. Computing the lid-driven cavity test problem with the WCSPH approach, we have found that the standard implementation of the no-slip boundary condition by the ghost-particle approach [3] may cause the stability problems. Our proposal to overcome these difficulties is based on the combination of the free-slip and no-slip boundary conditions. The detailed discussion of this problem is presented in Sect. 6.

2. Formulation of the SPH method

The main idea behind SPH is the introduction of the kernel interpolants for the field quantities so that the fluid dynamics is represented by particle evolution equations. The SPH method is based on three approximations.

The first is interpolation of the field quantities at a point. To construct it, we utilize an integral interpolant $\hat{A}(\mathbf{r})$ of any field $A(\mathbf{r})$ (for simplicity we consider here a scalar field)

$$\hat{A}(\mathbf{r}) = \int_{\Omega} A(\mathbf{r}') W(\mathbf{r} - \mathbf{r}', h) d\mathbf{r}', \quad (1)$$

where the integration is over all the domain Ω and $W(\mathbf{r}, h)$ is a weighting function (the kernel) with the parameter h called the smoothing length (a linear dimension of smoothing). Generally, the kernel should possess a symmetrical form

$$W(\mathbf{r}, h) = W(-\mathbf{r}, h), \quad (2)$$

satisfy the limit condition

$$\lim_{h \rightarrow 0} W(\mathbf{r}, h) = \delta(\mathbf{r}), \quad (3)$$

where $\delta(\mathbf{r})$ is the Dirac delta distribution, and should be normalized so that

$$\int_{\Omega} W(\mathbf{r}, h) d\mathbf{r} = 1. \quad (4)$$

Additionally, the kernel should be at least as many times differentiable as the field A . Taking into consideration the computational effort and the proper implementation of the boundary conditions (Sect. 6), it is

worth to use compact support kernels. Since there are a lot of possibilities to choose $W(\mathbf{r}, h)$, we decided to compare solutions obtained employing three different 2D kernels (Sect. 7.1): the cubic B-spline form

$$W(\mathbf{r}, h) = \frac{10}{7\pi h^2} \begin{cases} 1 - \frac{3}{2}q^2 + \frac{3}{4}q^3, & \text{for } 0 \leq q \leq 1, \\ \frac{1}{4}(2 - q)^3, & \text{for } 1 \leq q \leq 2, \\ 0, & \text{otherwise,} \end{cases} \quad (5)$$

the quintic form proposed by Wendland [10]

$$W(\mathbf{r}, h) = \frac{7}{4\pi h^2} \begin{cases} (1 - \frac{q}{2})^4 (2q + 1), & \text{for } |\mathbf{r}| \leq 2h, \\ 0, & \text{otherwise,} \end{cases} \quad (6)$$

and the quintic B-spline form introduced by Morris [11]

$$W(\mathbf{r}, h) = \frac{7}{478\pi h^2} \begin{cases} (3 - q)^5 - 6(2 - q)^5 + 15(1 - q)^5, & \text{for } 0 \leq q \leq 1, \\ (3 - q)^5 - 6(2 - q)^5, & \text{for } 1 \leq q \leq 2, \\ (3 - q)^5, & \text{for } 2 \leq q \leq 3, \\ 0, & \text{otherwise,} \end{cases} \quad (7)$$

where $q = |\mathbf{r}|/h$.

The second approximation of the SPH technique is the discretization of space. It is done through dividing the domain into a fine-grained representation (particles). Each particle carries the properties of the field. The integral interpolant $\widehat{(\cdot)}$, Eq. (1), becomes then the summation interpolant $\langle \cdot \rangle$

$$\langle A \rangle(\mathbf{r}) = \sum_b A(\mathbf{r}_b) W(\mathbf{r} - \mathbf{r}_b, h) \Omega_b, \quad (8)$$

where \mathbf{r}_b and Ω_b denote the position and volume of the particle b . The SPH task involves the foregoing computations of the interpolant at each particle, so that Eq. (8) may be rewritten into the common form

$$\langle A \rangle_a = \sum_b A_b W_{ab}(h) \Omega_b, \quad (9)$$

where $\langle A \rangle_a = \langle A \rangle(\mathbf{r}_a)$, $A_a = A(\mathbf{r}_a)$ and $W_{ab}(h) = W_{ba}(h) = W(\mathbf{r}_b - \mathbf{r}_a, h)$.

An additional advantage of SPH reveals with the differentiation of fields. In accordance with (1), the gradient of $A(\mathbf{r})$ assumes the form

$$\widehat{\nabla A}(\mathbf{r}) = \int_{\Omega} \nabla A(\mathbf{r}') W(\mathbf{r} - \mathbf{r}', h) d\mathbf{r}'. \quad (10)$$

Taking advantage of the integration by parts rule and utilizing the kernel symmetry, we can transform the foregoing equation into

$$\widehat{\nabla A}(\mathbf{r}) = \int_{\partial\Omega} A(\mathbf{r}') W(\mathbf{r} - \mathbf{r}') \mathbf{n}' dS + \int_{\Omega} A(\mathbf{r}') \nabla' W(\mathbf{r} - \mathbf{r}', h) d\mathbf{r}', \quad (11)$$

where $\mathbf{n}' = \mathbf{n}(\mathbf{r}')$ is the normal vector to surface $\partial\Omega$. Generally, the first term does not necessarily vanish for finite domain sizes, cf. [12]. However, it is a common practice to neglect this term and deal with the boundaries explicitly. The SPH form (discretization) of (11) brings the common rule

$$\langle \nabla A \rangle_a = \sum_b A_b \nabla_a W_{ab}(h) \Omega_b. \quad (12)$$

Since the nabla operator acts only on the kernel, the gradient of the field is dependent only on the values of the fields at particles, not gradients.

The third SPH feature is the assumption that the field value A_a at a point and its SPH approximation $\langle A \rangle$ are in relation

$$\langle A \rangle_a \approx A_a. \quad (13)$$

Since, in the case of the time dependent simulations, for each time step, the calculation of the field quantities is performed using the results obtained in the previous step, the above introduced assumption becomes natural.

3. Governing equations

The full set of governing equations for incompressible viscous flow is composed of the Navier-Stokes (N-S) equation

$$\frac{d\mathbf{u}}{dt} = -\frac{1}{\rho}\nabla p + \nu\nabla^2\mathbf{u} + \mathbf{f}, \quad (14)$$

where $\rho = \text{const}$ is the density, \mathbf{u} the velocity, t the time, p the pressure, ν the kinematic viscosity and \mathbf{f} an external force, and the continuity equation

$$\frac{d\rho}{dt} = -\rho\nabla \cdot \mathbf{u}, \quad (15)$$

that for $\rho = \text{const}$ arises to the form

$$\nabla \cdot \mathbf{u} = 0. \quad (16)$$

The whole set of governing equations should be expressed in the SPH formalism. Utilizing the relation (12), the divergence of velocity becomes

$$\langle \nabla \cdot \mathbf{u} \rangle_a = \sum_b \mathbf{u}_b \cdot \nabla_a W_{ab}(h)\Omega_b. \quad (17)$$

Therefore, the continuity equation (15) takes the form

$$\frac{d\rho_a}{dt} = -\rho_a \sum_b \frac{m_b}{\rho_b} \mathbf{u}_b \cdot \nabla_a W_{ab}(h), \quad (18)$$

where $m_b/\rho_b = \Omega_b$. It is important to note that various ways exist to express the divergence, for example,

$$\frac{d\rho_a}{dt} = \sum_b m_b \mathbf{u}_{ab} \cdot \nabla_a W_{ab}(h), \quad (19)$$

where $\mathbf{u}_{ab} = \mathbf{u}_a - \mathbf{u}_b$. The advantage of the above form over (18) is the symmetry with swapping particles a and b . Therefore, in practice, it is more accurate to use (19) [13]. However, there exists an alternative formulation. The fluid density can be computed directly from the SPH formula (9)

$$\rho_a = \sum_b \rho_b W_{ab}(h)\Omega_b = \sum_b m_b W_{ab}(h). \quad (20)$$

A practical disadvantage of this approach is that ρ must be evaluated by summing over the particles before other quantities [11]. Therefore, the computational effort increases (Sect. 7.1). Another disadvantage is the problem with representing sharp discontinuities near material interfaces. To avoid this difficulty, Hu & Adams [14] suggested to use the form

$$\rho_a = m_a \sum_b W_{ab}(h). \quad (21)$$

In the SPH technique, the pressure N-S term is responsible for ensuring the incompressibility constraint (Sect. 4). Utilizing (12) it takes the form

$$\left\langle \frac{1}{\varrho} \nabla p \right\rangle_a = \frac{1}{\varrho_a} \sum_b \frac{m_b}{\varrho_b} p_b \nabla_a W_{ab}(h). \quad (22)$$

Similarly to the continuity equation (19) there is a possibility to obtain more useful gradient approximations. In the present paper, we utilize the form proposed by Colagrossi and Landrini [15]

$$\left\langle \frac{1}{\varrho} \nabla p \right\rangle_a = \sum_b m_b \frac{p_a + p_b}{\varrho_a \varrho_b} \nabla_a W_{ab}(h). \quad (23)$$

is expressed as a combination of the finite difference and SPH discretisations [16] [17]. For the present work, we utilize the form (with a small regularising parameter $\eta = 0.01h$) [17]

$$\langle \nabla(\nu \nabla \cdot \mathbf{u}) \rangle_a = \sum_b m_b \left(8 \frac{\nu_a + \nu_b}{\varrho_a + \varrho_b} \frac{\mathbf{u}_{ab} \cdot \mathbf{r}_{ab}}{r_{ab}^2 + \eta^2} \right) \nabla_a W_{ab}(h). \quad (24)$$

Since SPH is fully Lagrangian approach, the particle advection equation completes the system

$$\frac{d\mathbf{r}_a}{dt} = \mathbf{u}_a. \quad (25)$$

4. Incompressibility treatment

To compute incompressible flows in the Eulerian CFD, two approaches are commonly used: the artificial compressibility method (where a specific equation of state is applied) and the pressure-correction technique (where the velocity field is projected onto the divergence-free space). Generally, the analogs of these techniques are also used in the SPH approach. They are presented in the following.

4.1. Weakly Compressible SPH

The most common technique is the weakly compressible SPH (WCSPH). It involves the set of governing equations closed by a suitably chosen, artificial equation of state $p = p(\varrho)$. Since the fluid pressure is an explicit function of ϱ , the density gradient exerts an influence on the particle motion. The commonly used equation of state has the form [18]

$$p = \frac{c^2 \varrho_0}{\gamma} \left[\left(\frac{\varrho}{\varrho_0} \right)^\gamma - 1 \right], \quad (26)$$

where the reference density ϱ_0 , the numerical sound speed c and parameter γ are suitably chosen to reduce the density fluctuations down to demanded level. In the present work, to assure density variations lower than 1%, we set $\gamma = 7$ and c at the level at least 10 times higher than the maximal fluid velocity [19]. However, since the sound speed is high, the time step should be, correspondingly, very small (cf. Sect. 5). Therefore, the computational efficiency is the main weakness of the WCSPH method.

4.2. Truly Incompressible SPH with the grid-projected Poisson solver

The newest promising technique is the truly incompressible SPH (ISPH). It is based on the Projection Method which is a common approach for numerically solving time-dependent incompressible fluid-flow problems. In this technique the pressure needed to ensure incompressibility is found by projecting the calculated velocity field onto the divergence-free space [3]. This is possible due to the Helmholtz decomposition which states: every vector field \mathbf{A} that is twice continuously differentiable and vanishes faster than $1/r$ at infinity can be decomposed into the gradient and the curl parts as follows [20]

$$\mathbf{A} = \nabla \phi + \nabla \times \mathbf{B} = \mathbf{A}_{\text{curl free}} + \mathbf{A}_{\text{div free}}, \quad (27)$$

where ϕ and \mathbf{B} are suitably chosen and

$$\begin{aligned}\nabla \times \mathbf{A}_{\text{curl free}} &= \nabla \times (\nabla \phi) = 0, \\ \nabla \cdot \mathbf{A}_{\text{div free}} &= \nabla \cdot (\nabla \times \mathbf{B}) = 0.\end{aligned}\tag{28}$$

In the ISPH approach, the decomposition procedure begins with splitting the integration of the N-S equation (14) on the time interval $\delta t = t^{n+1} - t^n$ into two parts. The first, so-called predictor step, gives the fractional velocity \mathbf{u}^*

$$\frac{\mathbf{u}^* - \mathbf{u}^n}{\delta t} = \nu \nabla^2 \mathbf{u}^n + \mathbf{f}^n.\tag{29}$$

The right-hand side of the above equation contains all the N-S terms except the one connected with the pressure. The second part of the procedure is the correction step

$$\frac{\mathbf{u}^{n+1} - \mathbf{u}^*}{\delta t} = -\frac{1}{\varrho} \nabla p^{n+1}.\tag{30}$$

It imposes the correction of \mathbf{u}^* to ensure compliance with the divergence-free constraint. To obtain an appropriate pressure p^{n+1} we write the divergence of Eq. (30)

$$\nabla \cdot \left(\frac{\mathbf{u}^{n+1} - \mathbf{u}^*}{\delta t} \right) = \nabla \cdot \left(-\frac{1}{\varrho} \nabla p^{n+1} \right).\tag{31}$$

Since we expect a divergence-free velocity field at the end of the time step, we require that $\nabla \cdot \mathbf{u}^{n+1} = 0$. Therefore, the formula (31) arises into the Poisson equation

$$\nabla \cdot \left(\frac{1}{\varrho} \nabla p^{n+1} \right) = \frac{\nabla \cdot \mathbf{u}^*}{\delta t}.\tag{32}$$

Now, the correction step (30), performed with p^{n+1} obtained from the above relation, yields the divergence-free velocity field.

The common way to solve the Poisson equation in the SPH approach is to compute it directly on particles (irregular grid), cf. Sect. 4.3. However, there exists another, less useful (specially for free-surface flows), but much more efficient treatment, called here the Grid-Projected Poisson Solver (GPPS). It consists in projecting the r.h.s. of (32) on an auxiliary grid and then to crunch it with some commonly known (from Eulerian approaches) solvers. This is a standard technique in various particle methods (more precisely, particle-mesh methods) such as Lagrangian PDF or Vortex-in-Cell.

4.3. Truly incompressible SPH with the particle Poisson solver

Employing together the SPH divergence and gradient operators, it is straightforward to obtain the direct SPH representation of the Laplace operator on the l.h.s. of (32). However, Cummins & Rudman [3] performed a simple one-dimensional hydrostatic test to show that such an approach produces a distinct pressure decoupling pattern. To avoid this problem, it is common to utilize the approximate Laplacian operator with the similar form as the viscous N-S term (24)

$$\left\langle \nabla \cdot \frac{1}{\varrho} \nabla p \right\rangle_a \approx \sum_b \frac{m_b}{\varrho_a} \frac{4}{\varrho_a + \varrho_b} \frac{p_{ab} \mathbf{r}_{ab} \cdot \nabla_a W_{ab}(h)}{r_{ab}^2 + \eta^2},\tag{33}$$

where $p_{ab} = p_a - p_b$. The pressure gradient is here computed using a finite-difference approximation. In this concept the Poisson equation (32) is solved on the irregular grid of Lagrangian points (particles); therefore, this variant of ISPH will be called here the Particle Poisson Solver (PPS).

However, the main disadvantage of the PPS (Sect. 7.1) is its inefficiency. Dealing with the Poisson equation using Eq. (33) consists in solving a linear equation system with a sparse irregular coefficient matrix. It requires much more CPU time and memory than the Poisson solvers performed on a regular grid.

5. Time step criteria

In the way to assure the stability of the SPH scheme, several time step criteria must be satisfied [3] [11] [17] [21]. In the case of the ISPH approach, the CFL time step condition is

$$\delta t \leq 0.25 \frac{h}{|\mathbf{u}|_{max}}, \quad (34)$$

where $|\mathbf{u}|_{max}$ is maximal velocity in the flow. In the WCSPH approach, due to the utilization of the equation of state (26), the CFL time step condition is

$$\delta t \leq 0.25 \frac{h}{c + |\mathbf{u}|_{max}}. \quad (35)$$

Since we demand density fluctuations to be lower than 1%, we have chosen $c \geq 10|\mathbf{u}|_{max}$ (Sect. 4.1). Therefore, when the flow is not dominated by viscous or external forces, WCSPH is computationally less efficient than the ISPH approaches. In the case of explicit schemes for viscous flows, another stability criterium is

$$\delta t \leq 0.125 \frac{h^2}{\nu}. \quad (36)$$

Additional condition must be satisfied due to the magnitude of particle accelerations \mathbf{f}

$$\delta t \leq 0.25 \min_a \left(\frac{h}{|\mathbf{f}_a|} \right)^{\frac{1}{2}}. \quad (37)$$

6. Boundary conditions

The proper implementation of the boundaries is one of the common topics in the SPH developments during recent years. Early stage applications of WCSPH involved high Reynolds number simulations with free-slip boundaries, performed using one layer of boundary particles placed at the wall. The layer exerted a strong repulsive force to prevent penetrating solid surfaces [22]. Since the number of interacting particles near the walls is decreased, the accuracy of numerical scheme degrades. Another treatment was proposed by Campbell [23] where the boundary condition was included in (11) through the residual boundary term. Today, the most often used boundary conditions are based on dummy particles [4] [24]. They are regularly distributed on the boundaries and have prescribed velocity during the whole simulation (no-slip condition). In ISPH, the Poisson equation (32) is solved on these dummy particles as well to repulse the fluid. To prevent inconsistency between density of inner particles and that of the wall, an additional set of dummy particle layers is placed outside the domain. Other popular, virtual-particle based boundary conditions utilize so-called mirror particles. These particles are given the prescribed velocity to assure the proper boundary condition. But, their properties are not integrated in time, unlike those of real SPH particles. Nowadays, there are two commonly used mirror-particle approaches. The first, developed by Morris [11], consists in the combination of dummy and mirror particles. The velocity of inner particles is suitably projected on fixed boundary particles. Then, the boundary particles interact with the fluid. The second approach, so-called Multiple Boundary Tangent method, is similar to the previous one but the procedure of projecting particle velocities is different [25].

The mirror-particle techniques, presented above, have been further developed to another, more natural approach, i.e., the ghost particle method [3]. This technique is similar to the Classic Image Problem in electrostatics [20] [26]. To any particle a located at \mathbf{r}_a near the straight and infinite boundary, we introduce the image a' of this particle located at

$$\mathbf{r}_{a'} = 2\mathbf{d} + \mathbf{r}_a \quad (38)$$

where \mathbf{d} is the vector pointing from the particle to the nearest point at the wall, cf. Fig. 1(a). Since a chosen kernel is compact, the boundary may be finite. The role of these particles is to assure a high accuracy of the

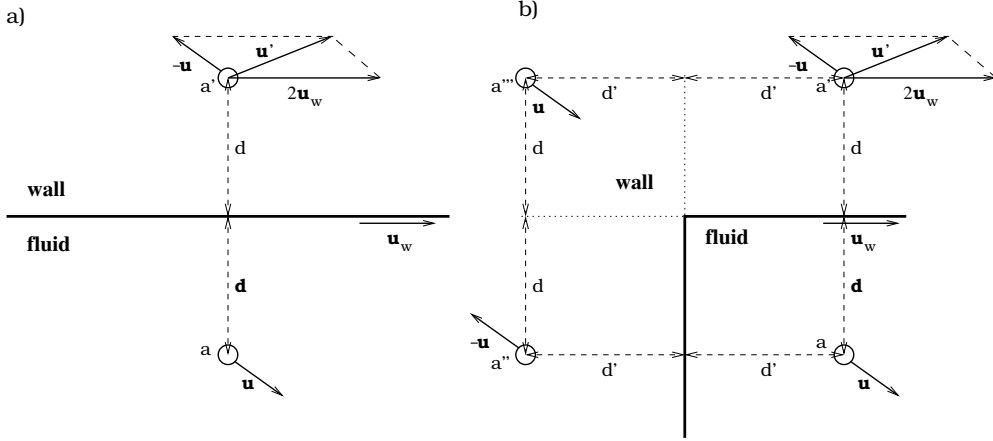


Figure 1: The ghost-particle no-slip boundary scheme: a) straight wall, b) inner corner.

computation (to remedy the lack of particles near the boundaries) and to enforce the boundary condition for the field quantities. Thus, the natural way to obtain the proper implementation of the boundary condition, with the no-slip condition for velocity field, is to set:

$$\mathbf{u}_{a'} = 2\mathbf{u}_w - \mathbf{u}_a, \quad m_{a'} = m_a, \quad \varrho_{a'} = \varrho_a, \quad (39)$$

where \mathbf{u}_w is the velocity of the boundary. To enforce the proper Neumann boundary condition for the pressure

$$\frac{\partial p}{\partial n} = 0, \quad (40)$$

where \mathbf{n} is the vector normal to the boundary, we extend the set (39) by an approximation of (40)

$$p_{a'} = p_a. \quad (41)$$

Let \mathbf{r}_w stand for a position of any point placed at the boundary. Due to the kernel symmetry we have

$$W(\mathbf{r}_w - \mathbf{r}_a, h) = W(\mathbf{r}_w - \mathbf{r}_{a'}, h). \quad (42)$$

Now, utilizing the SPH summation interpolant (9) for velocity, we write

$$\begin{aligned} \langle \mathbf{u} \rangle (\mathbf{r}_w) &= \sum_a \frac{m_a}{\varrho_a} \mathbf{u}_a W(\mathbf{r}_w - \mathbf{r}_a, h) + \sum_{a'} \frac{m_{a'}}{\varrho_{a'}} (2\mathbf{u}_w - \mathbf{u}_a) W(\mathbf{r}_w - \mathbf{r}_{a'}, h) = \\ &= 2\mathbf{u}_w \sum_a \frac{m_a}{\varrho_a} W(\mathbf{r}_w - \mathbf{r}_a, h). \end{aligned} \quad (43)$$

Since the summation in the above equation is over fluid particles only, assuming nearly homogeneous distribution of fluid particles, we have

$$\sum_a \frac{m_a}{\varrho_a} W(\mathbf{r}_w - \mathbf{r}_a, h) \approx \frac{1}{2} \quad (44)$$

and (43) becomes

$$\langle \mathbf{u} \rangle (\mathbf{r}_w) \approx \mathbf{u}_w. \quad (45)$$

Therefore, (39) provides the proper formulation of the no-slip condition.

Another boundary type that can be treated with the ghost-particle approach is an inner corner. The technique of constructing particle images is presented in Fig. 1(b). In this case we have to use three mirror particles. It is important to note that the influence range of this corner is smaller than $2h$. For a larger

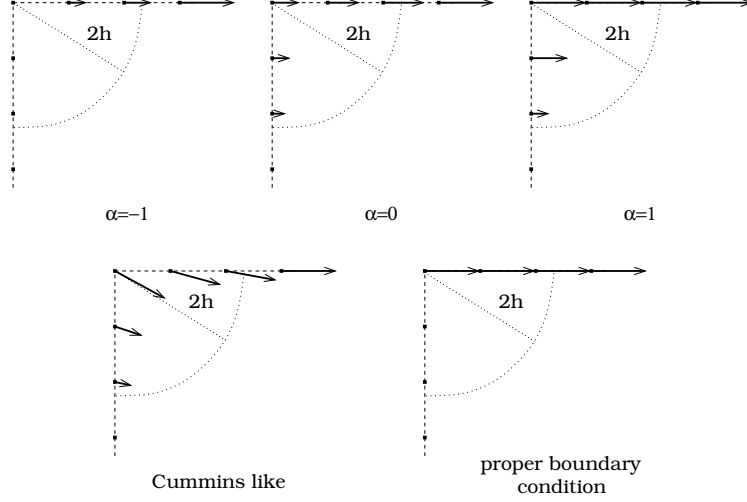


Figure 2: The problem with the ghost-particle no-slip boundary condition near the corner: depending on value of the parameter α , the velocity boundary condition changes.

distance from the corner, the boundary condition boils down to the previous case (both in vertical and horizontal directions). For the distances smaller than $2h$, Cummins and Rudman [3] use the third particle placed symmetrically in respect to the corner point possessing the same density and mass but opposite velocity to fluid particle. Since the velocity vector computed at the corner is non-zero in the case of not moving boundaries, this formulation is improper. Therefore, in the way to find a more accurate approach, we parametrize the mirror particles' properties as follows (using the notation from Fig. 1):

$$\begin{aligned}
 \varrho_a = \varrho_{a'} = \varrho_{a''} = \varrho_{a'''}, & \quad \mathbf{u}_{a'} = 2\mathbf{u}_w - \mathbf{u}_a, & \quad \mathbf{r}_{a'} = 2\mathbf{d} + \mathbf{r}_a, \\
 m_a = m_{a'} = m_{a''} = m_{a'''}, & \quad \mathbf{u}_{a''} = -\mathbf{u}_a, & \quad \mathbf{r}_{a''} = 2\mathbf{d}' + \mathbf{r}_a, \\
 & \quad \mathbf{u}_{a'''} = 2\alpha\mathbf{u}_w + \mathbf{u}_a, & \quad \mathbf{r}_{a'''} = 2\mathbf{d} + 2\mathbf{d}' + \mathbf{r}_a,
 \end{aligned} \tag{46}$$

where α may change from -1 up to 1 . Now, for a point \mathbf{r}_w at the boundary, we may carry similar investigation as in (43)

$$\begin{aligned}
 \langle \mathbf{u} \rangle (\mathbf{r}_w) &= \sum_a \frac{m_a}{\varrho_a} \mathbf{u}_a W(\mathbf{r}_w - \mathbf{r}_a, h) + \sum_{a'} \frac{m_{a'}}{\varrho_{a'}} (2\mathbf{u}_w - \mathbf{u}_{a'}) W(\mathbf{r}_w - \mathbf{r}_{a'}, h) \\
 &+ \sum_{a''} \frac{m_{a''}}{\varrho_{a''}} \mathbf{u}_{a''} W(\mathbf{r}_w - \mathbf{r}_{a''}, h) + \sum_a \frac{m_{a'''}}{\varrho_{a'''}} (2\mathbf{u}_w \alpha + \mathbf{u}_{a'''}) W(\mathbf{r}_w - \mathbf{r}_{a'''}, h) \\
 &= 2\mathbf{u}_w \sum_a \frac{m_a}{\varrho_a} [W(\mathbf{r}_w - 2\mathbf{d} + \mathbf{r}_a, h) + \alpha W(\mathbf{r}_w - 2\mathbf{d} - 2\mathbf{d}' + \mathbf{r}_a, h)].
 \end{aligned} \tag{47}$$

For a point placed exactly at the corner, the above equation reduces to the form

$$\langle \mathbf{u} \rangle (\mathbf{r}_{\text{corner}}) \approx \frac{1}{2} \mathbf{u}_w (1 + \alpha). \tag{48}$$

Depending on value of the parameter α , the velocity of the corner changes from $\mathbf{u}(\mathbf{r}_{\text{corner}}) = \mathbf{0}$ (for $\alpha = -1$) up to $\mathbf{u}(\mathbf{r}_{\text{corner}}) = \mathbf{u}_w$ (for $\alpha = 1$). Despite this parametrization, there is no way to assure proper velocity at boundary that is closer than $2h$ from the corner. This issue is presented in Fig. 2. Yet, the simulations of various test problems show that varying parameter α does not have a significant impact on the global (except near the corner) velocity or density fields. Therefore, in the present work, we utilize the no-slip condition with $\alpha = 0$.

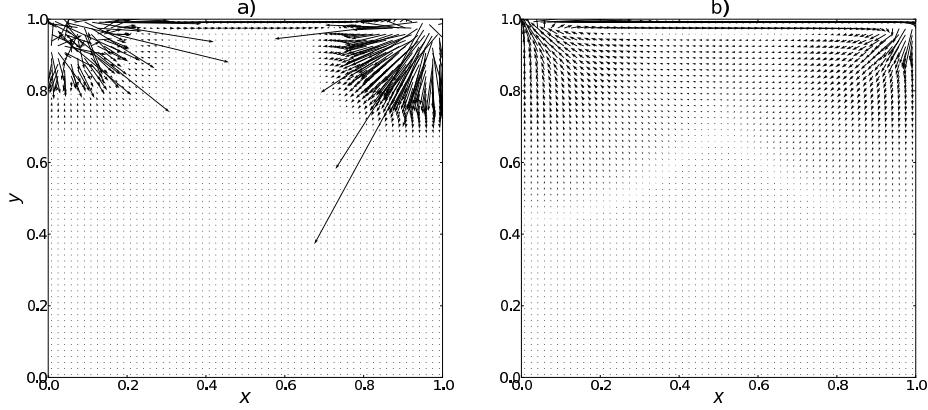


Figure 3: The WCSPH results of the lid-driven cavity ($Re = 1000$) at $t = 0.03$ with: a) the no-slip and b) the free-slip boundary treatment for velocity divergence computation; employing no-slip condition induces instabilities near the corners.

Another problem with the no-slip condition implementation appears during computation of density in WCSPH utilizing the continuity equation (15). Assuming a statistically homogeneous distribution of particle positions, the velocity component tangential to the boundary is negligible for computing the divergence. Therefore, along straight boundaries the no-slip condition is properly stated. The problem appears near the corners. Utilizing (12), we may compute the divergence of velocity at the boundary near the corner

$$\begin{aligned} \langle \nabla \cdot \mathbf{u} \rangle (\mathbf{r}_w) = & \sum_a \frac{m_a}{\varrho_a} \mathbf{u}_a \cdot \nabla_a W(\mathbf{r}_w - \mathbf{r}_a, h) + \sum_{a'} \frac{m_{a'}}{\varrho_{a'}} \mathbf{u}_{a'} \cdot \nabla_{a'} W(\mathbf{r}_w - \mathbf{r}_{a'}, h) \\ & + \sum_{a''} \frac{m_{a''}}{\varrho_{a''}} \mathbf{u}_{a''} \cdot \nabla_{a''} W(\mathbf{r}_w - \mathbf{r}_{a''}, h) + \sum_{a'''} \frac{m_{a'''}}{\varrho_{a'''}} \mathbf{u}_{a'''} \cdot \nabla_{a'''} W(\mathbf{r}_w - \mathbf{r}_{a'''}, h). \end{aligned} \quad (49)$$

For the point \mathbf{r}_c that is placed in the fluid $\varepsilon \rightarrow 0$ away from the corner we have

$$\begin{aligned} \nabla_a W(\mathbf{r}_c - \mathbf{r}_a, h) \cdot \mathbf{n}_x = \nabla_{a'} W(\mathbf{r}_c - \mathbf{r}_{a'}, h) \cdot \mathbf{n}_x = \\ -\nabla_{a''} W(\mathbf{r}_c - \mathbf{r}_{a''}, h) \cdot \mathbf{n}_x = -\nabla_{a'''} W(\mathbf{r}_c - \mathbf{r}_{a'''}, h) \cdot \mathbf{n}_x \end{aligned} \quad (50)$$

and

$$\begin{aligned} \nabla_a W(\mathbf{r}_c - \mathbf{r}_a, h) \cdot \mathbf{n}_y = -\nabla_{a'} W(\mathbf{r}_c - \mathbf{r}_{a'}, h) \cdot \mathbf{n}_y = \\ \nabla_{a''} W(\mathbf{r}_c - \mathbf{r}_{a''}, h) \cdot \mathbf{n}_y = -\nabla_{a'''} W(\mathbf{r}_c - \mathbf{r}_{a'''}, h) \cdot \mathbf{n}_y, \end{aligned} \quad (51)$$

where \mathbf{n}_x and \mathbf{n}_y are unit vectors in x and y directions respectively. Therefore, connecting the above relations with (49) and (46) we obtain

$$\langle \nabla \cdot \mathbf{u} \rangle (\mathbf{r}_c) \approx 0. \quad (52)$$

Let us consider the situation where fluid particles are driven to the corner. To prevent penetrating the boundary, there should appear a repulsive force near this corner. In WCSPH this is done by a local density increase. However, since the divergence of velocity is always close to zero near the corner, according to the continuity equation (15), the density does not change. This may induce a growth of velocity instabilities near the corners (see Fig. 3). Therefore, only for computing the divergence of velocity, we suggest to use the free-slip condition. For a straight boundary, cf. Fig. 4, the free-slip mirror particle is placed at $\mathbf{r}_{a'} = 2\mathbf{d} + \mathbf{r}_a$. It has the same mass and density, its velocity component normal to the boundary is opposite, while the tangential component is unchanged. At the corner, cf. Fig. 4(b), the mirror particles carry the following

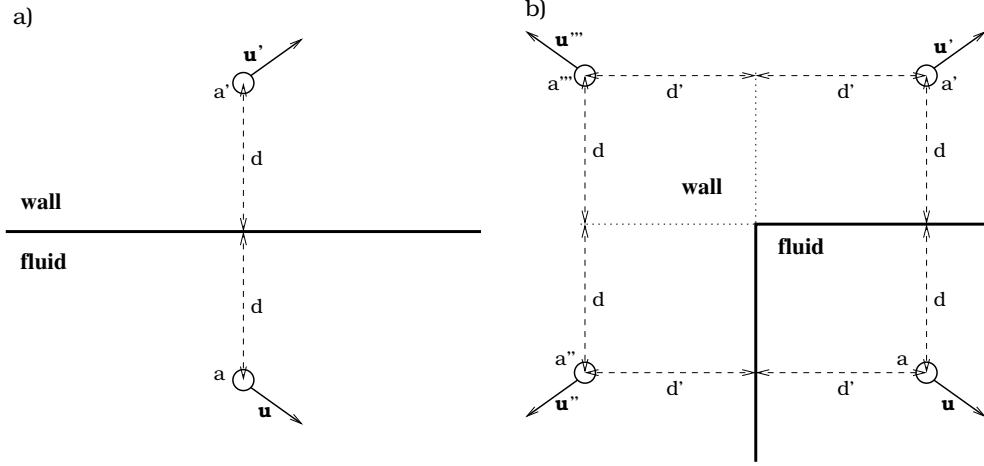


Figure 4: The ghost-particle free-slip boundary treatment for: a) the straight wall and b) the corner.

properties:

$$\begin{aligned}
\rho_a &= \rho_{a'} = \rho_{a''} = \rho_{a'''}, \\
m_a &= m_{a'} = m_{a''} = m_{a'''}, & \mathbf{u}_{a'} \cdot \mathbf{n}_x &= \mathbf{u}_a \cdot \mathbf{n}_x, & \mathbf{u}_{a'} \cdot \mathbf{n}_y &= -\mathbf{u}_a \cdot \mathbf{n}_y, \\
\mathbf{r}_{a'} &= 2\mathbf{d} + \mathbf{r}_a, & \mathbf{u}_{a''} \cdot \mathbf{n}_x &= -\mathbf{u}_a \cdot \mathbf{n}_x, & \mathbf{u}_{a'} \cdot \mathbf{n}_y &= \mathbf{u}_a \cdot \mathbf{n}_y, \\
\mathbf{r}_{a''} &= 2\mathbf{d}' + \mathbf{r}_a, & \mathbf{u}_{a'''} \cdot \mathbf{n}_x &= -\mathbf{u}_a \cdot \mathbf{n}_x, & \mathbf{u}_{a'} \cdot \mathbf{n}_y &= -\mathbf{u}_a \cdot \mathbf{n}_y. \\
\mathbf{r}_{a'''} &= 2\mathbf{d} + 2\mathbf{d}' + \mathbf{r}_a,
\end{aligned} \tag{53}$$

Obviously, this kind of boundary treatment presented here is basically limited to flat wall segments only; more advanced formulations exist and represent the state of the art for arbitrarily-shaped boundaries, e.g., [12]. However, since the main focus of our paper is on incompressibility treatments, we have chosen simple geometry cases to have enough reference data.

7. Velocity error measurement

7.1. Lid-driven cavity

The lid-driven cavity is a common test of numerical algorithms for viscous flows. It involves a fluid at density ρ_0 inside a square ($L \times L$) box where only one boundary moves with the constant velocity \mathbf{u}_w . The geometry is very simple, however there is no analytical solution. In the present work, we computed the lid-driven cavity flow at $Re = |\mathbf{u}_w|L/\nu = 1000$. For this value of Reynolds number the flow is still laminar and there is no necessity to use a turbulence model. All results are suitably non-dimensionalised with L , $|\mathbf{u}_w|$, ρ_0 (especially time is normalized with the convective time scale $L/|\mathbf{u}_w|$) and compared to those from a numerical calculation on a fine grid performed with the Eulerian solver by Ghia et al. [27].

7.1.1. The kernel type influence

One of the important issues that has an impact on the SPH solutions is a proper selection of the kernel. To compare the treatments of the incompressibility constraint, we decided to perform the benchmark simulation of the lid-driven cavity flow with the three kernels presented in Sect. 2. The particles' number has been chosen with two requirements: N should be large enough to get solutions comparable to reference data (yet not fully converged); however, it should be sufficiently small to show kernels' defects. We decided to use $N = 3600$ particles in the domain and $h/\Delta r = 2$, cf. Sect. 7.1.2. The steady-state solution velocity profiles are presented in Fig. 5. The results performed with the cubic spline kernel are the most inconsistent with the reference data. This discrepancy is caused by the particles' clustering phenomenon. Figs. 6 and 7 respectively present particles' spatial distribution and histograms of the distance between the nearest pairs of particles

for all mentioned kernels. As it transpires from the histogram for the cubic spline kernel, in this case there are many particles that move joined in groups, cf. also details in Fig. 6; as a consequence, the accuracy of the scheme is radically decreased. As far as the quintic kernels are concerned, both perform similarly to each other. However, the kernel proposed by Morris et al. (7) shows a more pronounced tendency to clustering (Fig. 7); moreover, it is not zero up to $|\mathbf{r}|/h = 3$ (as contrasted to $|\mathbf{r}|/h = 2$ for the other kernels), so it involves many more particles. Therefore, the computational time is increased about 12% comparing to the Wendland kernel. Summarizing, due to a good agreement with the reference data, not noticeable clustering phenomenon, and finally the efficiency, for the further analysis we decided to use the quintic Wendland kernel. An interesting work about its behavior in SPH has recently been performed by Robinson [28] (Ch. 7).

7.1.2. The kernel size influence

Apart from the initial inter-particle distance Δr (related to the number of particles in the domain), in the SPH approach there exists another characteristic length - the kernel parameter h . Examining the impact on the solutions, we decided to compute the lid-driven cavity problem ($Re = 1000$) for chosen $N = 3600$, the Wendland kernel and different $h/\Delta r$ values. Figure 8 presents the velocity profiles for $h/\Delta r = 2.31, 2.0, 1.67$ and 1.5 computed with all the SPH incompressibility variants. In comparison to the Ghia et al. reference data, there is no significant effect of the kernel size on the velocity field. However, since the parameter $h/\Delta r$ determines the number of particles under the kernel hat, the number of interaction between particles (and the computational effort) grow like $\sim (h/\Delta r)^D$, where D is the space dimension. Weighting between the computational times and the accuracy, for all simulations presented henceforth, we decided to use $h/\Delta r = 2.0$.

7.1.3. The particle number influence

Examining the influence of the spatial resolution, the simulations were performed with a different number of particles in the domain (from $N = 1600$ up to $N = 57600$). The steady-state velocity profiles are presented in Fig. 9. In all the methods of incompressibility treatment, the profiles obtained for $N = 1600$ did not agree very well with the Ghia solution [27] obtained on 129×129 Eulerian mesh. Performing simulations with the higher resolutions, the accuracy increases so that in the case of $N = 14400$, independently on the compressibility treatment, the obtained results are in very good agreement with the reference simulations. For $N = 57600$ the velocity profiles computed using WCSPH and ISPH - PPS approaches practically overlap with the Ghia's reference data. Unfortunately, the ISPH - GPPS solution is not so accurate as we expect. This deficiency is due to a higher numerical diffusion caused by the projection of the quantities from particles on a regular grid.

Due to the utilization of the equation of state and the time step constraint in the WCSPH approach, the CPU time of the lid-driven cavity simulation computed by the ISPH method with PPS is about 7 times shorter. On the other hand, performing the ISPH-GPPS simulations, the computational effort may be reduced about 15 times. The comparison of CPU times for all considered SPH schemes is presented in Fig. 10.

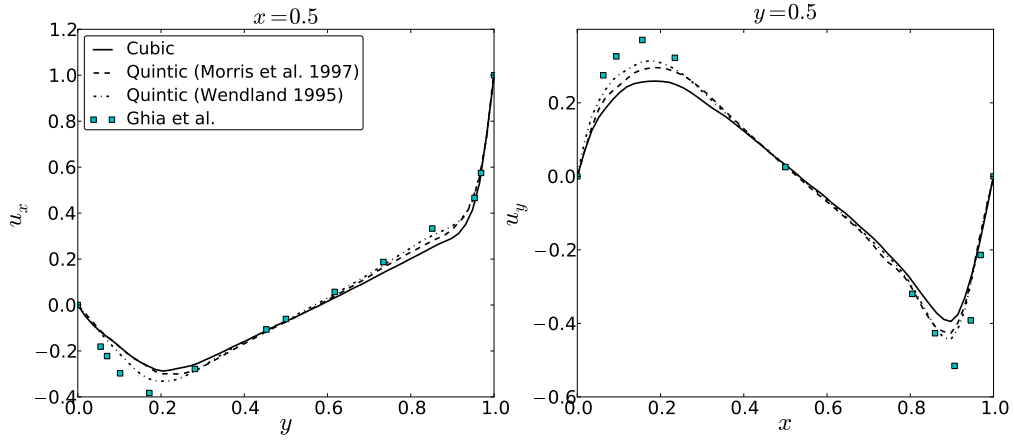
7.2. The Rayleigh-Taylor instability

The Rayleigh-Taylor instability is one of generic multi-phase flows, therefore it is commonly utilized as a test problem. It involves two immiscible fluids enclosed in a rectangular domain of width L and height $2L$. Initially, in our case, the phases are separated by the interface located at $y = 1 - 0.15 \sin(2\pi x)$. The lower component has density $\varrho_L = \varrho_0$, while the upper one $\varrho_U = 1.8\varrho_0$. Since the system is subject to gravity $\mathbf{g} = (0, -g)$ and the upper phase is heavier, in the absence of the surface tension an instability always arises and vorticity is generated. The Reynolds number may be defined as

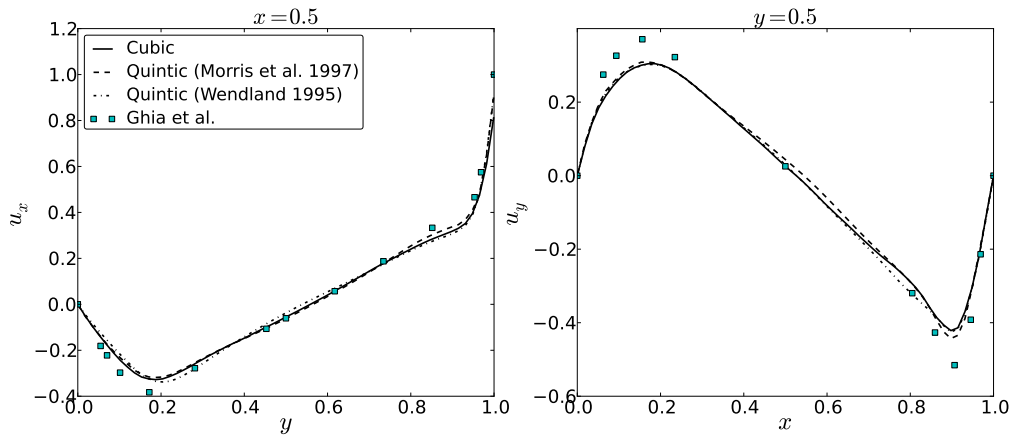
$$Re = \frac{\sqrt{L^3 g}}{\nu} = 420. \quad (54)$$

The simulations were performed for 120×240 particles in the domain. To compute the hydrostatic force, we use the technique described in [29], where the hydrostatic pressure is computed on a regular mesh and later

(a) WCSPH



(b) ISPH-GPPS



(c) ISPH-PPS

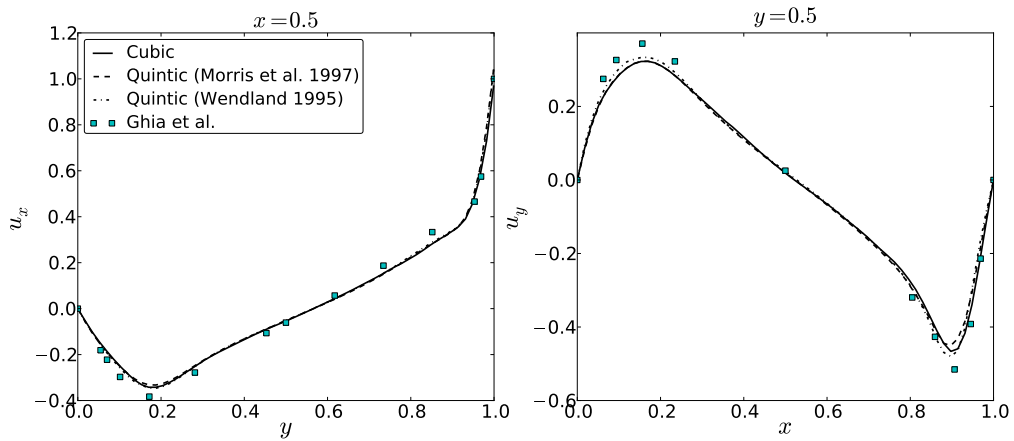


Figure 5: The lid-driven cavity steady-state velocity profiles for: (a) WCSPH, (b) ISPH-GPPS and (c) ISPH-PPS against Ghia et al. [27] results; profiles obtained for different kernels; $N = 3600$, $h/\Delta r = 2$.

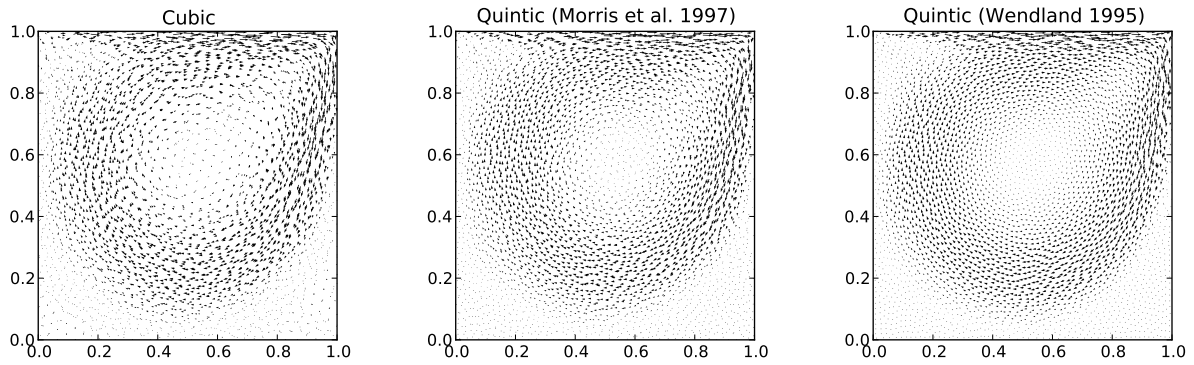


Figure 6: The lid-driven cavity steady-state solution ($Re = 1000$, $N = 3600$) computed with the WCSPH approach and kernels: (5), (6), (7); the particle clustering phenomenon is noticeable with the cubic spline kernel.

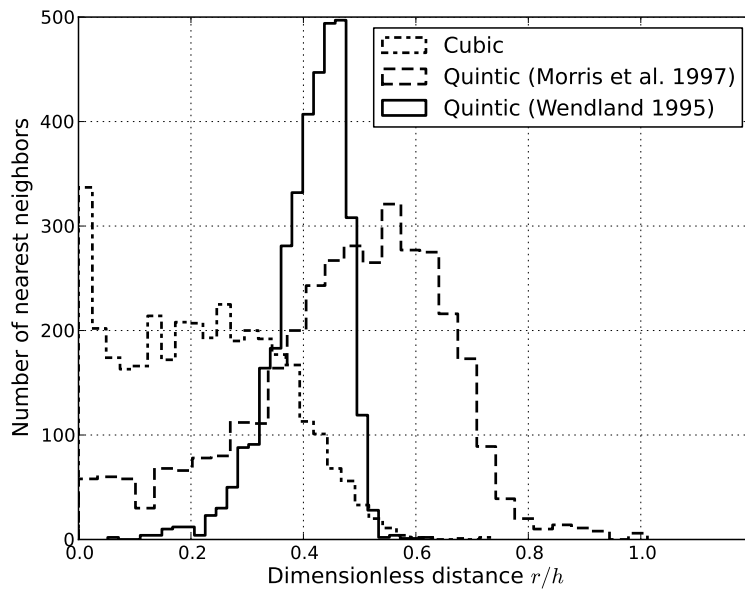
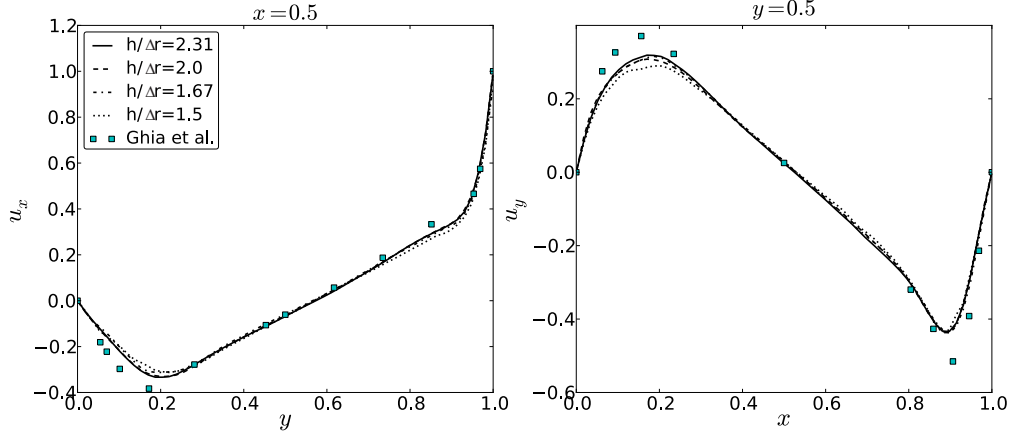
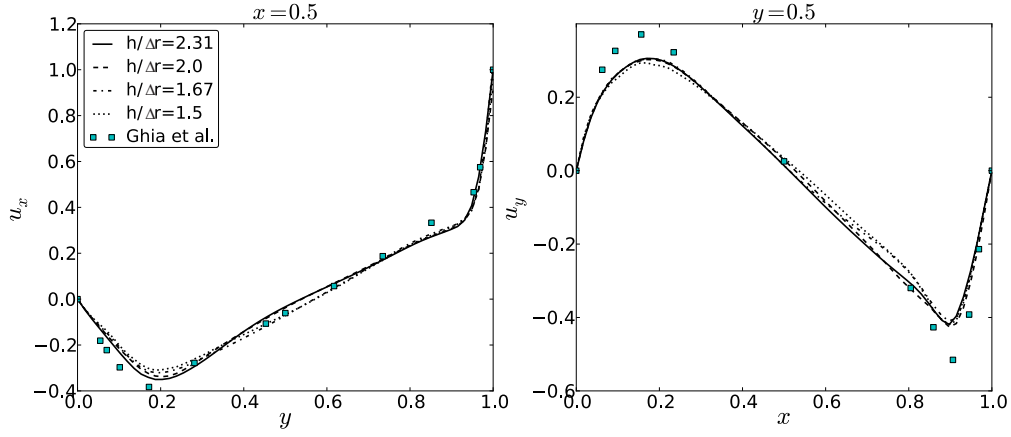


Figure 7: Histograms of the distance between the nearest pairs of particles; the results obtained for the WCSPH approach and kernels: (5), (6), (7).

(a) WCSPH



(b) ISPH-GPPS



(c) ISPH-PPS

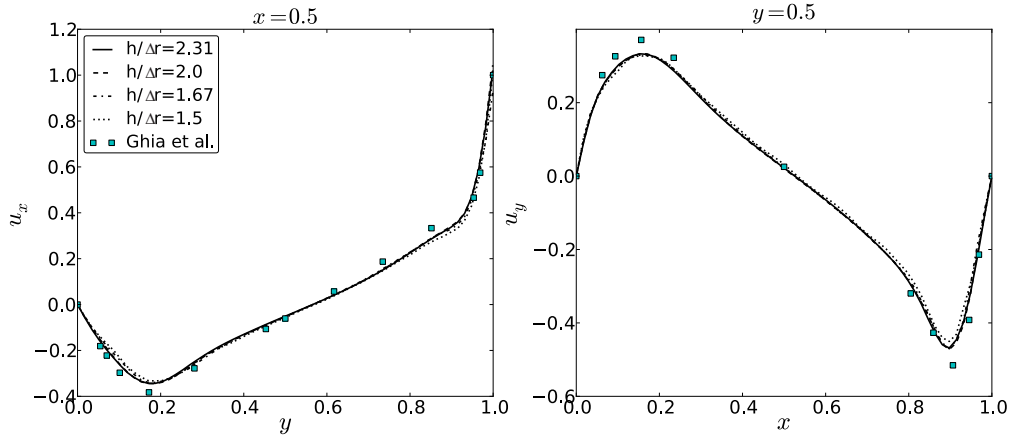
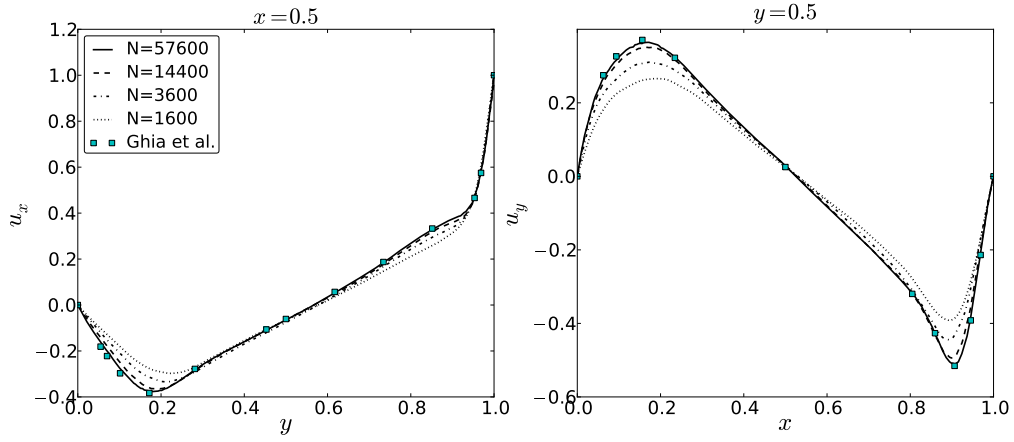
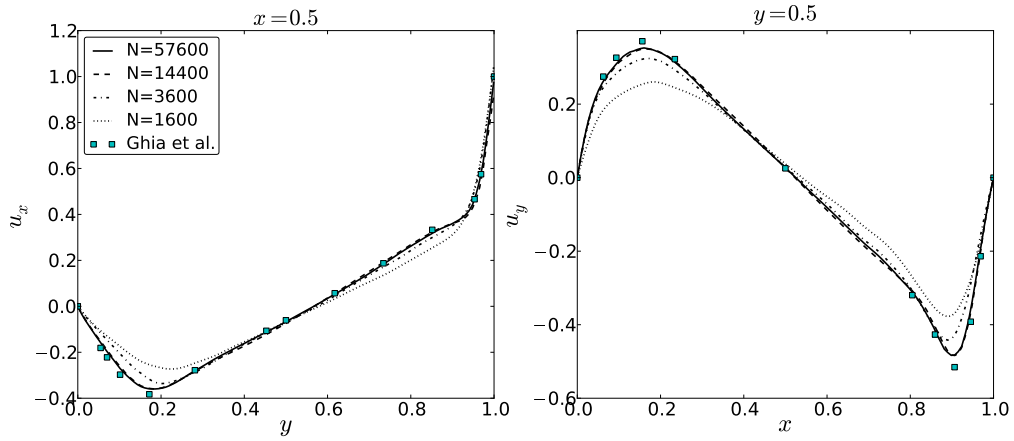


Figure 8: The lid-driven cavity steady-state velocity profiles for: (a) WCSPH, (b) ISPH-GPPS and (c) ISPH-PPS against Ghia et al. [27] results; profiles obtained with different $h/\Delta r$ values; results obtained using the Wendland kernel [10] and $N = 3600$ particles in domain.

(a) WCSPH



(b) ISPH-GPPS



(c) ISPH-PPS

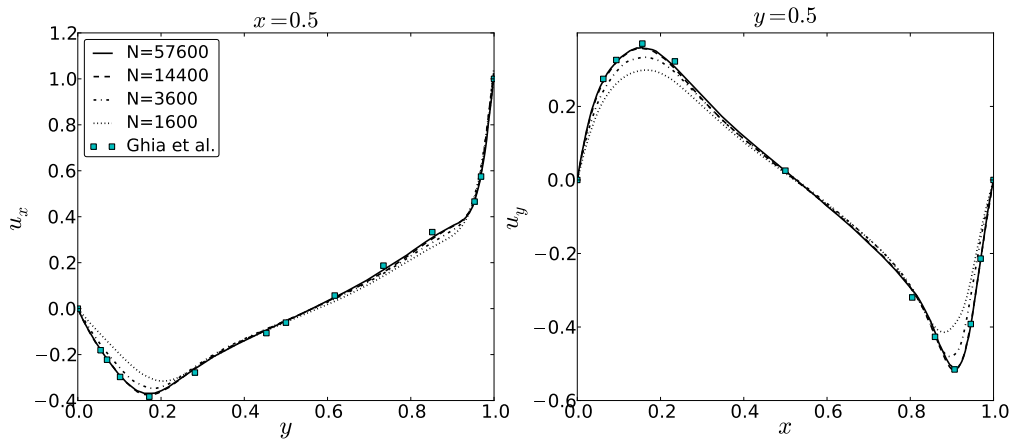


Figure 9: The lid-driven cavity steady-state velocity profiles for: (a) WCSPH, (b) ISPH-GPPS and (c) ISPH-PPS against Ghia et al. [27] results; results for different number of particles N ; data obtained using the Wendland kernel [10] and $h/\Delta r = 2$.

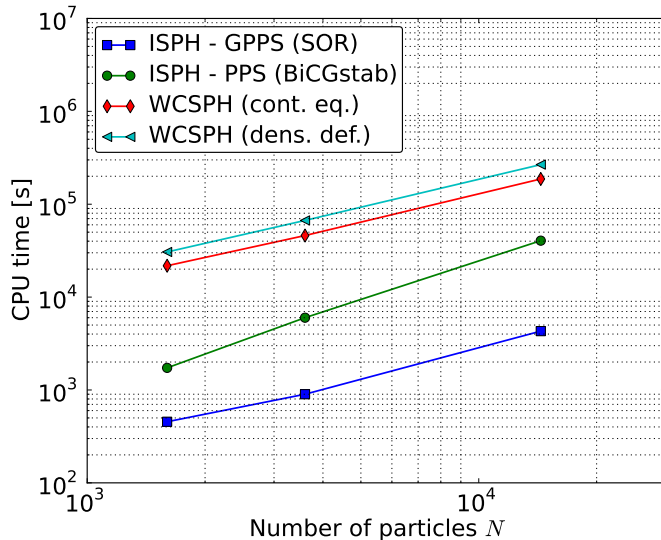


Figure 10: The CPU times to obtain the steady-state solution of the lid-driven cavity ($Re = 1000$) using the WCSPH and both ISPH approaches; for the WCSPH method, two continuity equations are compared: Eq. (19) and density definition (21).

projected on the particles. Figure 11 presents particle positions (directly showing the location of liquid-liquid interface) computed with different treatments of the incompressibility condition. All the simulations are compared to the reference solutions from the Level-Set method (312×624 cells) computed by Grenier et al. [30]. Presented data were obtained at $t = 5$ (normalized with the convective time scale $\sqrt{L/g}$).

Comparing the interface shapes, we find no convincing arguments to judge which SPH approach is more accurate. However, the comparison of the computational times shows that the most valuable choice is the ISPH-GPPS. The ISPH-PPS is slower about 6 times, while the WCSPH about 13 times.

8. Density error measurement

In order to measure the density estimation errors, we compute two quantities: the mean density over the flow domain $\bar{\varrho}(t)$ and the root mean square of the density fluctuations $\varrho_{\text{rms}}(t)$. However, since in the Projection Methods the values of the density carried by particles do not change, there is the necessity to use formulas which are able to compute $\bar{\varrho}(t)$ and $\varrho_{\text{rms}}(t)$ taking into account both the density values and spatial distribution of the particles. The simplest proposals (expressed in the SPH formulae) are: for the mean density

$$\bar{\varrho}(t) = \frac{1}{N} \sum_a m_a \sum_b W_{ab}(h), \quad (55)$$

and for the density fluctuations $\varrho_{\text{rms}}(t)$

$$\varrho_{\text{rms}}(t) = \sqrt{\frac{1}{N} \sum_a \left(m_a \sum_b W_{ab} - \bar{\varrho}(t) \right)^2}. \quad (56)$$

In WCSPH, comparing the influence of the kernel shape, we observe that the quintic kernel proposed by Wendland (6) gives the smallest fluctuations of the density field, cf. Fig. 12(a). The weakness of the Wendland kernel is a slight overestimation of the mean density. Even for a homogeneously distributed set of particles ($t = 0$) the density field is flawed, cf. discussion in [31]. At decrease of the $h/\Delta r$ parameter causes this error to grow from 0.2% for $h/\Delta r = 2.31$ up to about 0.8% for $h/\Delta r = 1.5$, cf. Fig. 12(b).

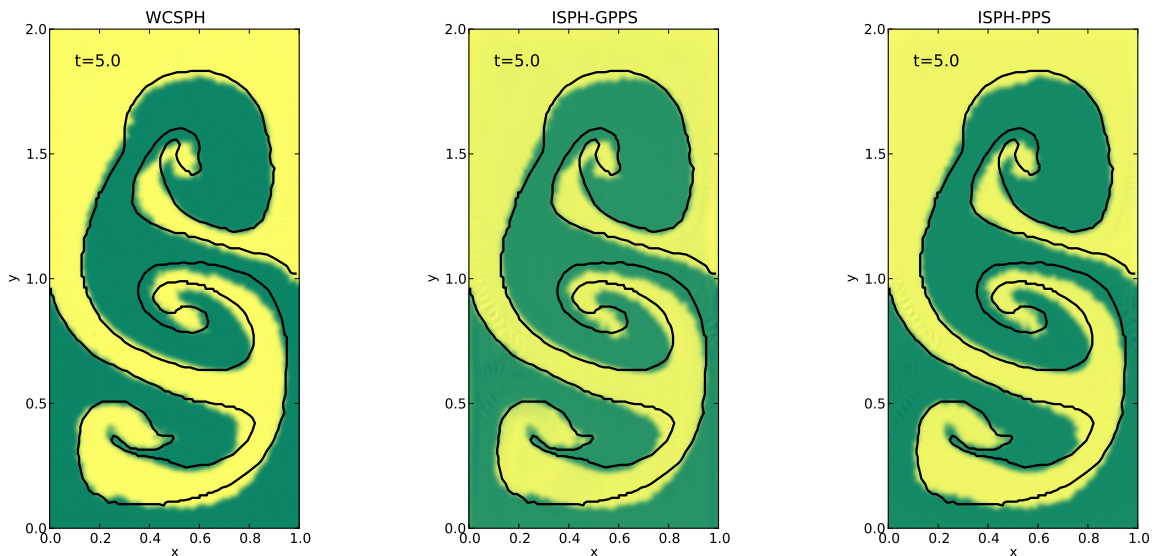


Figure 11: The Rayleigh-Taylor instability; particle positions at $t = 5$ obtained using different incompressibility treatments; solid line: liquid-liquid interface from the reference Level-Set solution [30].

Interestingly, parameter $h/\Delta r$ has no significant effect on $\varrho_{\text{rms}}(t)$. The particle number influence obtained with WCSPH is presented in Fig. 12(c). The density r.m.s. independently on the number of particles in domain, stabilizes after about $t = 1$ and remains less than 1% of initial density. Moreover, with increasing N the density r.m.s. goes down. In the case of ISPH solvers, the growth of the r.m.s. stops only after obtaining the steady-state solution (roughly at $t = 120$), cf. Fig. 12(d). Intriguing is the fact that for the ISPH approach, the increase of the number of particles N increases the r.m.s. For ISPH-PPS the r.m.s. of the steady-state solution changes: from 7% for $N = 1600$ up to 9% for $N = 14400$. For ISPH-GPPS the density field is additionally affected by the projections between the particles and the grid. These projections cause additional smoothing and the density field r.m.s. of the steady-state solution varies: for $N = 14400$ about 7%, for $N = 3600$ about 6% and $N = 1600$ about 5% of initial density.

This discrepancy between WCSPH and ISPH density error values is caused by the completely different mechanisms of computing the dynamical pressure in the Navier-Stokes equation. Since in the case of the WCSPH approach, the suitably-chosen equation of state is used, the density field suffers from short-scale density waves presented in Fig. 13(a). In the case of ISPH, there is no explicit correction to the density. Therefore, during the computations, the density field strongly deviates from the level of the initial state, cf. Fig. 13(b). Since the Projection Methods give such considerable density errors, it is meaningful to implement and an additional correction procedure, cf. Sect. 9.

In the case of the Rayleigh-Taylor instability, the comparison of density errors (cf. Fig. 14) shows similar behavior as in the lid-driven cavity case.

9. Constant-density ISPH approach

In the previous section we have shown that in the ISPH approach the density errors cumulate during computations. To solve this problem, Pozorski and Wawreńczuk [7] suggested to use the second correction term (a similar approach was later proposed, in the multi-phase flow context, by Hu and Adams [6]). Let us consider incompressible fluid with initially uniform density ϱ_0 . After the time step performed with the ISPH approach, the corrected velocity field satisfies the divergence-free condition; however, this procedure

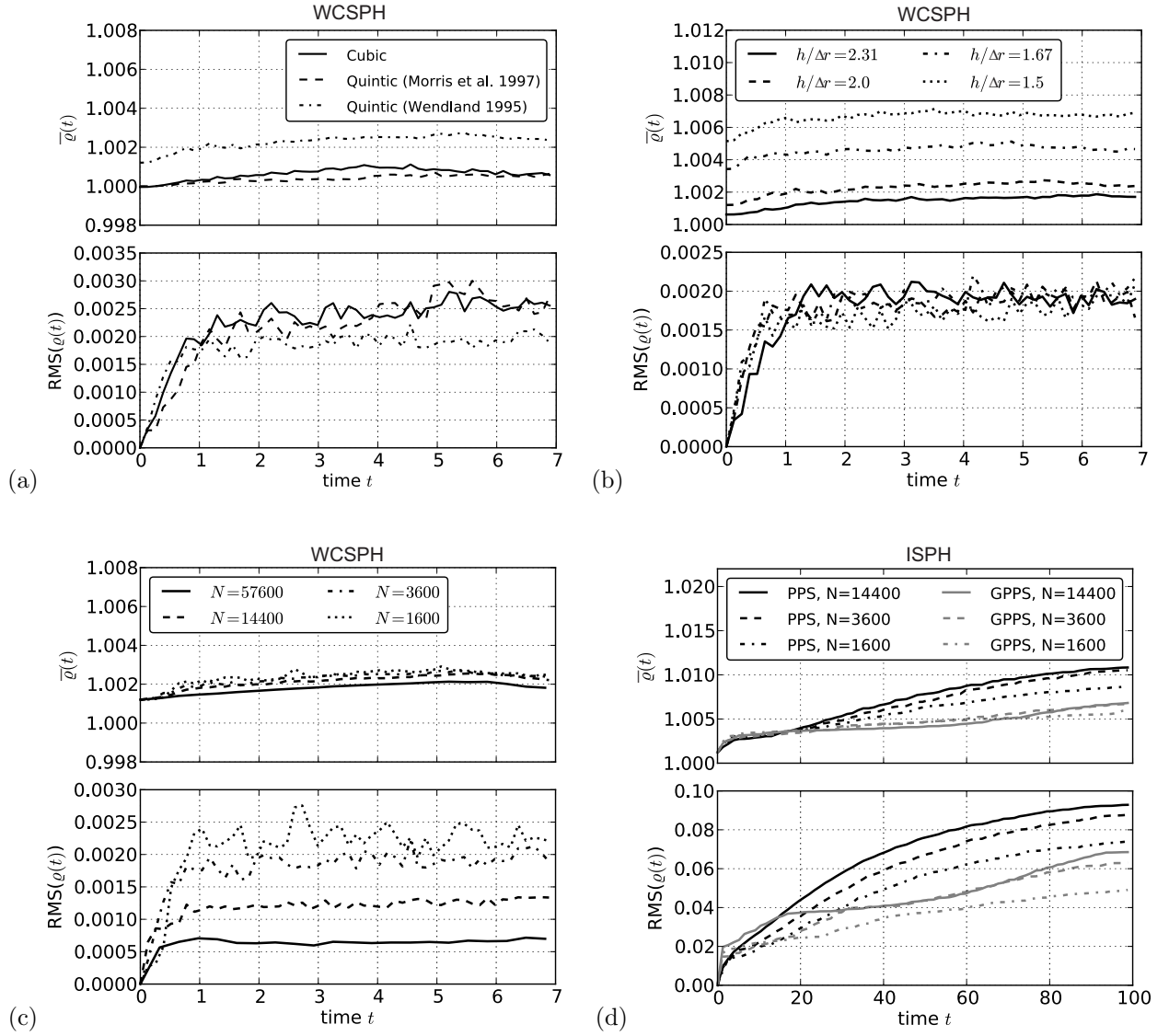


Figure 12: The density mean value and the r.m.s. obtained for the lid-driven cavity flow at $Re = 1000$; the effect of: (a) the kernel choice, (b) $h/\Delta r$, (c) number of particles N influence in the WCSPH approach; (d) particles number N influence in both: ISPH-PPS and ISPH-GPPS techniques.

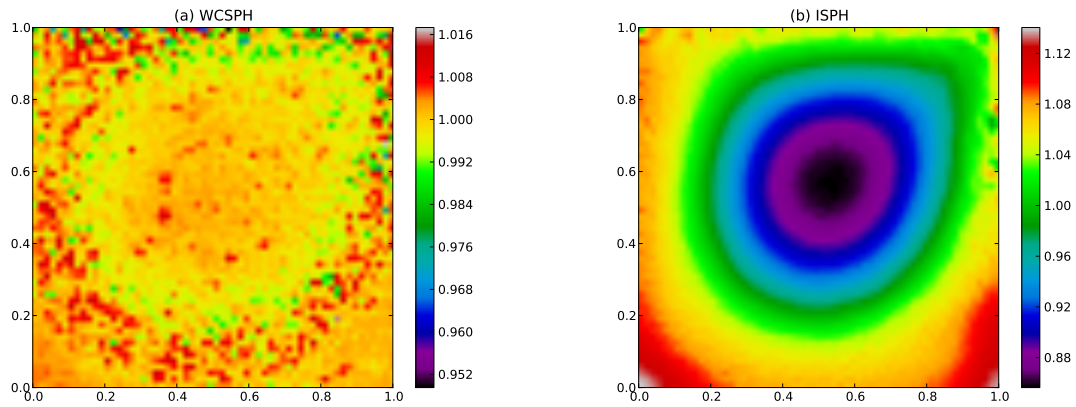


Figure 13: The lid-driven cavity flow: density field at the steady-state solution.

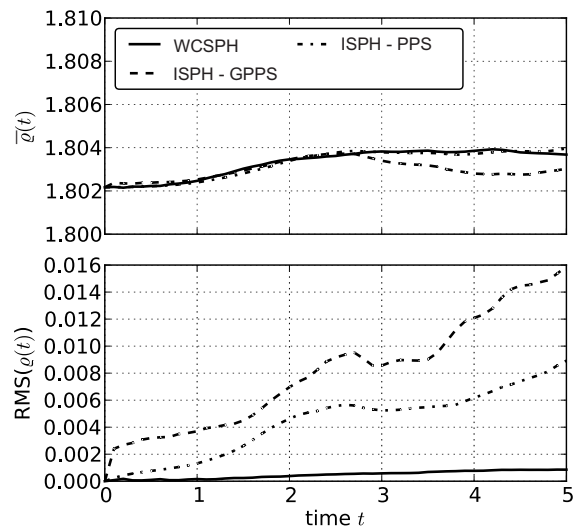


Figure 14: The density mean value and the r.m.s. obtained for the Rayleigh-Taylor instability (only upper phase $\varrho_U = 1.8\varrho_0$) using WCSPH and both ISPH approaches.

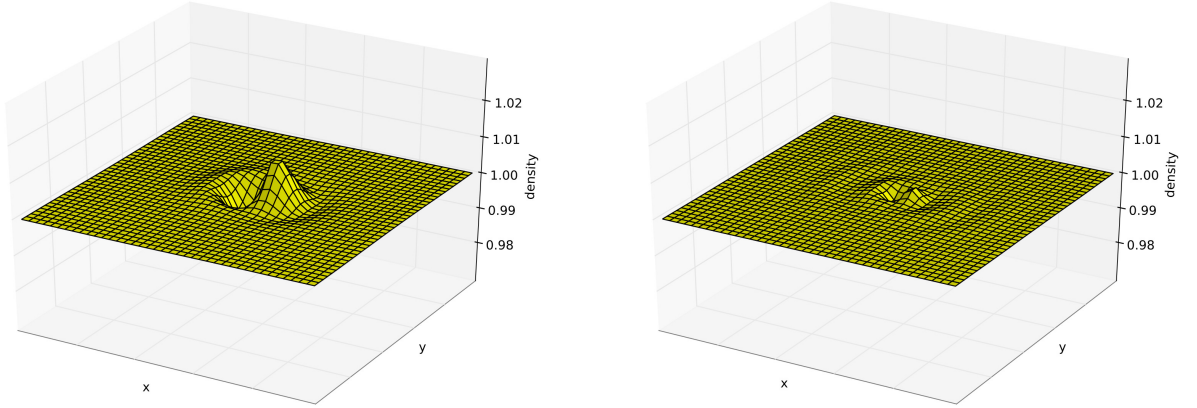


Figure 15: The density field with local disturbance; left: the initial state (regular set of particles with one particle displaced), right: after 50 correction iterations.

does not explicitly guarantee that $\varrho = \text{const}$. The Pozorski and Wawreńczuk idea consists in performing an additional correction to the particle positions

$$\mathbf{r}_a^{n+1} = \tilde{\mathbf{r}}_a^{n+1} - \frac{1}{\varrho_0} \nabla p_a^* = \mathbf{r}_a^n + \mathbf{u}_a^{n+1} \delta t - \frac{1}{\varrho_0} \nabla p_a^*, \quad (57)$$

where \mathbf{u}_a^{n+1} and $\tilde{\mathbf{r}}_a^{n+1}$ are respectively the divergence-free velocity field and particle positions obtained after the ISPH time step, Eqs. (30) and (32), while p_a^* appears as a potential correction field computed from

$$\frac{1}{\varrho_0} \nabla \cdot \left(\frac{\varrho^n}{\varrho_0} \nabla p^* \right) = 1 - \frac{\tilde{\varrho}^{n+1}}{\varrho_0}, \quad (58)$$

where $\tilde{\varrho}^{n+1}$ is the density obtained after the ISPH time step. Both ϱ^n and $\tilde{\varrho}^{n+1}$ are computed using Eq. (21). The Poisson Eq. (58) is obtained from the request

$$\varrho^{n+1}(\mathbf{r}_a) = m_a \sum_b W(\mathbf{r}_a - \mathbf{r}_b^{n+1}, h) = m_a \sum_b W(\mathbf{r}_a - \tilde{\mathbf{r}}_b^{n+1} - \nabla p_b^*, h) = \varrho_0(\mathbf{r}_a) \quad (59)$$

by the Taylor series expansion around $\mathbf{r}_a - \tilde{\mathbf{r}}_b^{n+1}$.

Since, performing such a correction, the second Poisson equation has to be solved, the computational effort is increased. However, there is no necessity to compute the correction at each time step; rather, it is applied only if the density error exceeds a certain threshold value. On the other hand, the procedure may be performed several times in one time step. Figure 15 shows how the initial disturbance of the density field (a regular set of particles with one particle displaced) is corrected with (58).

To perform the test problems, we decided to utilize ISPH with particle positions correction performed once per time step. Since both Poisson equations were solved on particles, we got fully grid-free approach. The velocity profiles of the lid-driven cavity problem ($Re = 1000$) are presented in Fig. 16. There are no noticeable differences between the velocities obtained using ISPH solver with (Fig. 16) and without (Fig. 9) the Pozorski and Wawreńczuk correction. However, comparing the density fields, cf. Fig. 17, with the results obtained without the correction, cf. Fig. 13(d), the advantages of this approach become obvious: the growth of the r.m.s. density stops after $t = 5$ and stays at a level less than 0.1%. The regularisation of the particles' distribution is also visible in the histograms of the distance to the nearest neighbor of each particle: the comparison of histograms for ISPH-PPS with and without the correction procedure is presented in Fig. 18. Another convincing argument for the utility of the Pozorski and Wawreńczuk approach is the computational effort. Since, as in the case of WCSPH, the density error does not accumulate, and, despite the use of two

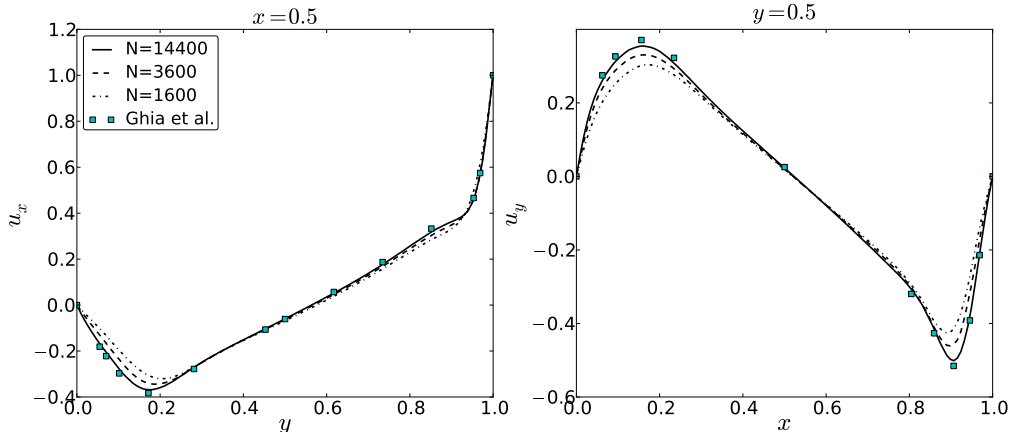


Figure 16: The lid-driven cavity velocity profiles at the steady-state against Ghia et al. [27] reference data ($Re = 1000$); results obtained using ISPH with PPS and Pozorski & Wawreńczuk correction [7] for the Wendland kernel [10], $h/\Delta r = 2$ and different number of particles N .

Poisson solvers, the computational time is about 3 times shorter (and about 2 times longer than ISPH-PPS), the use of the density correction algorithm seems to be profitable.

On the other hand, it is interesting to note a higher convergence rate with increasing number of particles in domain, as compared to the solutions obtained by Lee et al. [4] (Fig. 6) and Xu et al. [5] (Fig. 25). We suppose that a better convergence rate in our case is due to a proper choice of computational parameters ($h/\Delta r$, kernel type and b.c.).

For the Rayleigh-Taylor instability, the calculated particle positions at times $t = 1, 3$ and 5 are presented in Fig. 19. The comparison with the reference interface shapes [30] show quite a good agreement. What is more, there are no considerable differences between ISPH with and without the Pozorski and Wawreńczuk correction term. Moreover, as in the case of the lid-driven cavity, the use of such a correction term assures that the density error (Fig. 17) is kept below the desired level and the computational time is still acceptable (in comparison with the WCSPH approach).

10. Conclusions

In this paper three different SPH incompressibility treatments were considered. To validate these approaches, two tests cases were simulated: the lid-driven cavity at $Re = 1000$ and the Rayleigh-Taylor instability at $Re = 420$. Summarising, in comparison to the previous tests presented by Lee et al. [4] and Xu et al. [5], in all of the SPH incompressibility treatments, the velocity field exhibit a better convergence rate, when the number of particles in the domain grows. Detailed study of the incompressibility treatments revealed some pros and cons of the approaches. The main disadvantage of the WCSPH approach is its high computational cost. Therefore, from this point of view, it is better to use the ISPH approaches. Nevertheless, both the ISPH-GPPS and the ISPH-PPS solvers in their original formulation suffer from the density error accumulation.

For the fluid flows where besides the properly modelled velocity field, the correct density field is of importance, an interesting alternative to WCSPH is the ISPH approach with the separate density correction. In this approach the density accumulation error can be reduced to a specified level while still retaining the grid-free formulation. It is important to note that, as such, none of the ISPH approaches can be used to properly model gas-liquid flows such as a bubble raising in water, where the divergence-free condition is satisfied only for the liquid phase. Such flows can be relatively easily modelled with the WCSPH approach, where each phase can be computed with a different equation of state.

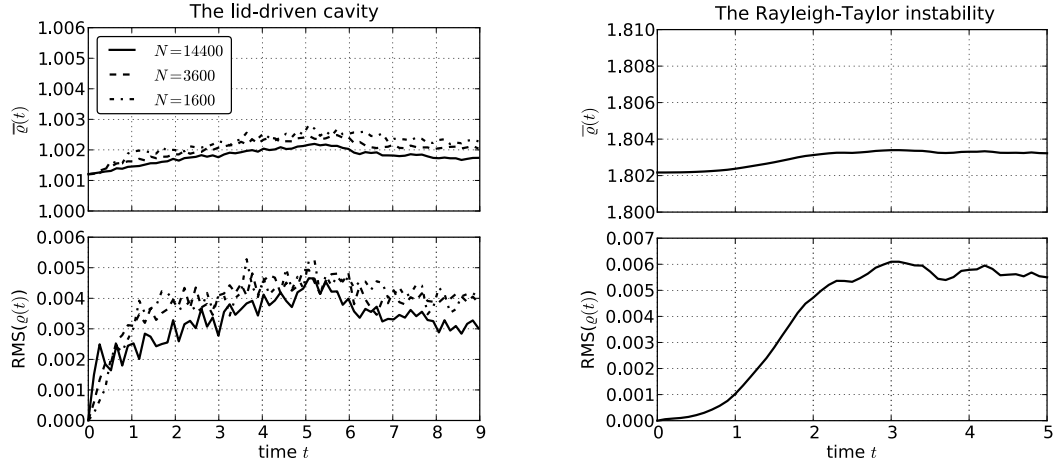


Figure 17: The density mean value and r.m.s. obtained using the ISPH approach with PPS and Pozorski & Wawreńczuk density correction [7]; (a) the lid driven cavity ($Re = 1000$), (b) the Rayleigh-Taylor instability ($Re = 420$); the results obtained for the Wendland kernel [10] and $h/\Delta r = 2$.

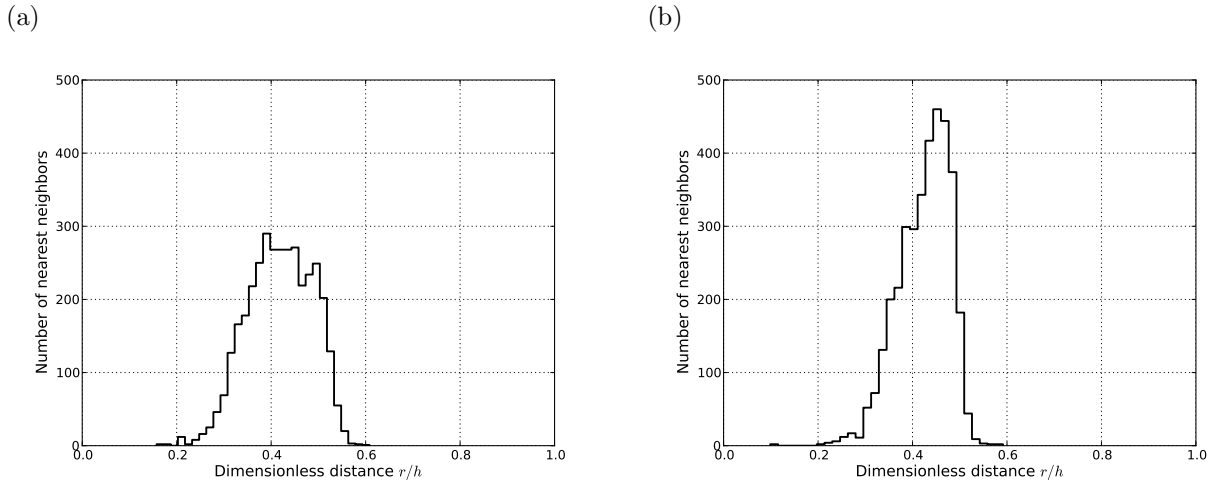


Figure 18: Histograms of the distance between the nearest pairs of the particles; the results obtained for the ISPH-PPS approach (a) without and (b) with the Pozorski and Wawreńczuk correction procedure.

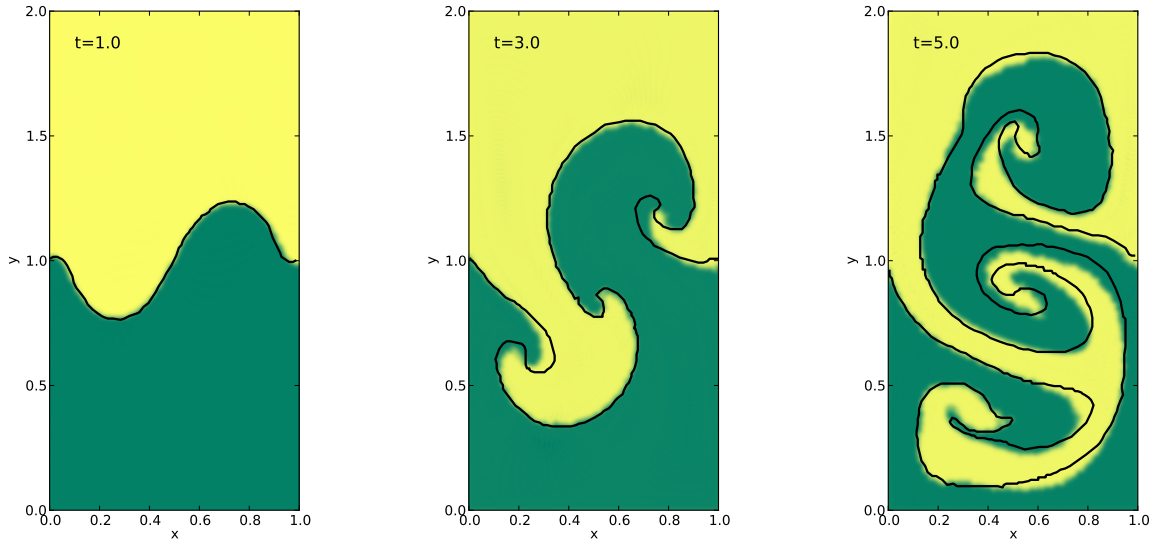


Figure 19: The Rayleigh-Taylor instability ($Re = 420$) computed using ISPH with PPS and Pozorski & Wawreńczuk density correction [7]; the black lines denote the interface position obtained by Grenier et al. [30] using the Level-Set formulation (312×624 cells).

The study has also shown the importance of correct choice of computational parameters: the kernel formula W , its smoothing length h for given inter-particle distance $h/\Delta r$, and the number of particles N in the domain. The impact of those parameters on the results has been analyzed and optimal kernel has been found (the Wendland formula). Regarding the other quantities, they represent a compromise between the CPU efficiency and accuracy. Further work will be undertaken to extend the ISPH approach making it possible to model gas-liquid mixed flows with the interface phenomena such as the surface tension or the Marangoni effect. Also, there is the need of appropriate wall b.c. for SPH simulations in complex geometries (arbitrary shape of the boundary).

References

- [1] R.A. Gingold, J.J. Monaghan, Smoothed Particle Hydrodynamics: Theory and application to non-spherical stars, *Mon. Not. R. Astron. Soc.* 181 (1977) 375-389.
- [2] L.B. Lucy, A numerical approach to the testing of the fission hypothesis, *Astron. J.* 82 (1977) 1013-1024.
- [3] S.J. Cummins, M. Rudman, An SPH projection method, *J. Comput. Phys.* 152 (1999) 584-607.
- [4] E.-S. Lee, C. Moulinec, R. Xu, D. Violeau, D. Laurence, P. Stansby, Comparisons of weakly compressible and truly incompressible algorithms for the SPH mesh free particle method, *J. Comput. Phys.* 227 (2008) 8417-8436.
- [5] R. Xu, P. Stansby, D. Laurence, Accuracy and stability in incompressible SPH (ISPH) based on the projection method and a new approach, *J. Comput. Phys.* 228 (2009) 6703-6725.
- [6] X.Y. Hu, N.A. Adams, An incompressible multi-phase SPH method, *J. Comput. Phys.* 227 (2007) 264-278.
- [7] J. Pozorski, A. Wawreńczuk, SPH computation of incompressible viscous flows, *J. Theor. Appl. Mech.* 40 (2002) 917-937.
- [8] J.-P. Minier, J. Pozorski, Wall boundary conditions in PDF methods and application to a turbulent flow, *Phys. Fluids* 11 (1999) 2632-2644.
- [9] A. Valizadeh, M. Shafieefar, J.J. Monaghan, S.A. Salehi Neyshaboori, Modeling two-phase flows using SPH method, *J. Applied Sci.* 8 (2008) 3817-3826.
- [10] H. Wendland, Piecewise polynomial, positive definite and compactly supported radial functions of minimal degree, *Adv. Comput. Math.* 4 (1995) 389-396.
- [11] J.P. Morris, P.J. Fox, Y. Zhu, Modeling low Reynolds number incompressible flows using SPH, *J. Comput. Phys.* 136 (1997) 214-226.
- [12] J. Feldman, J. Bonet, Dynamic refinement and boundary contact forces in SPH with applications in fluid flow problems, *Int. J. Numer. Meth. Engng.* 72 (2007) 295-324.

- [13] J.P. Morris, Analysis of Smoothed Particle Hydrodynamics with Applications, (doctor's thesis, Department of Mathematics, Monash University), 1996.
- [14] X.Y. Hu, N.A. Adams, A multi-phase SPH method for macroscopic and mesoscopic flows, *J. Comput. Phys.* 213 (2006) 844-861.
- [15] A. Colagrossi, M. Landrini, Numerical simulation of interfacial flows by smoothed particle hydrodynamics, *J. Comput. Phys.* 191 (2003) 227-264.
- [16] S.J. Cummins, M.J. Rudman, J.J. Monaghan, Projection methods and SPH, Monash University Applied Mechanics Report and Preprints, 1997.
- [17] P.W. Cleary, J.J. Monaghan, Conduction modelling using smoothed particle hydrodynamics, *J. Comput. Phys.* 148 (1999) 227-264.
- [18] G.K. Batchelor, An Introduction to Fluid Dynamics, Cambridge Univ. Press, 1967.
- [19] J.J. Monaghan, Simulating free surface flows with SPH, *J. Comput. Phys.* 110 (1994) 399-406.
- [20] D.J. Gryffits, Introduction to Electrodynamics - 3rd ed., Prentice Hall, New Jersey, 1999.
- [21] J.J. Monaghan, Smoothed Particle Hydrodynamics, *Annu. Rev. Astron. Astrophys.* 30 (1992) 542-574.
- [22] J.J. Monaghan, On the problem of penetration in particle methods, *J. Comput. Phys.* 82 (1989) 1-15.
- [23] P.M. Campbell, Some new algorithms for boundary value problems in smoothed particle hydrodynamics, Technical Report NA-TR-88-296, Mission Research Corporation, Albuquerque, 1989.
- [24] S. Shao, E.Y. Lo, Incompressible SPH method for simulating Newtonian and non-Newtonian flows with a free surface, *Adv. Water Resour.* 26 (2003) 787-800.
- [25] M. Yildiz, R.A. Rook, A. Suleman, SPH with multiple boundary tangent method, *Int. J. Numer. Meth. Engng.* 77 (2009) 14161438.
- [26] J.C. Maxwell, A treatise on electricity and magnetism, Clarendon Press, Oxford, 1873.
- [27] U. Ghia, K.N. Ghia, C.T. Shin, High Re-solution for incompressible flow using the Navier-Stokes equations and a multigrid method, *J. Comput. Phys.* 48 (1982) 387-411.
- [28] M. Robinson, Turbulence and Viscous Mixing using Smoothed Particle Hydrodynamics, PhD thesis, Monash University, Australia, 2009.
- [29] K. Szewc, J. Pozorski, A. Tanière, Modeling of natural convection with Smoothed Particle Hydrodynamics: Non-Boussinesq formulation, *Int. J. Heat Mass Transfer* 54 (2011) 4807-4816.
- [30] N. Grenier, M. Antuono, A. Colagrossi, D. Le Touzé, B. Alessandrini, An Hamiltonian interface SPH formulation for multi-fluid and free-surface flows, *J. Comput. Phys.* 228 (2009) 8380-8393.
- [31] J. Hongbin, D. Xin, On criterions for smoothed particle hydrodynamics kernels in stable field, *J. Comput. Phys.* 202 (2005) 699-709.

List of figure captions

Fig. 1: The ghost-particle no-slip boundary scheme: a) straight wall, b) inner corner.

Fig. 2: The problem with the ghost-particle no-slip boundary condition near the corner: depending on value of the parameter α , the velocity boundary condition changes.

Fig. 3: The WCSPH results of the lid-driven cavity ($Re = 1000$) at $t = 0.03$ with: a) the no-slip and b) the free-slip boundary treatment for velocity divergence computation; employing no-slip condition induces instabilities near the corners.

Fig. 4: The ghost-particle free-slip boundary treatment for: a) the straight wall and b) the corner.

Fig. 5: The lid-driven cavity steady-state velocity profiles for: (a) WCSPH, (b) ISPH-GPPS and (c) ISPH-PPS against Ghia et al. [27] results; profiles obtained for different kernels; $N = 3600$, $h/\Delta r = 2$.

Fig. 6: The lid-driven cavity steady-state solution ($Re = 1000$, $N = 3600$) computed with the WCSPH approach and kernels: (5), (6), (7); the particle clustering phenomenon is noticeable with the cubic spline kernel.

Fig. 7: Histograms of the distance between the nearest pairs of particles; the results obtained for the WCSPH approach and kernels: (5), (6), (7).

Fig. 8: The lid-driven cavity steady-state velocity profiles for: (a) WCSPH, (b) ISPH-GPPS and (c) ISPH-PPS against Ghia et al. [27] results; profiles obtained with different $h/\Delta r$ values; results obtained using the Wendland kernel [10] and $N = 3600$ particles in domain.

Fig. 9: The lid-driven cavity steady-state velocity profiles for: (a) WCSPH, (b) ISPH-GPPS and (c) ISPH-PPS against Ghia et al. [27] results; results for different number of particles N ; data obtained using the Wendland kernel [10] and $h/\Delta r = 2$.

Fig. 10: The CPU times to obtain the steady-state solution of the lid-driven cavity ($Re = 1000$) using the WCSPH and both ISPH approaches; for the WCSPH method, two continuity equations are compared: Eq. (19) and density definition (21).

Fig. 11: The Rayleigh-Taylor instability; particle positions at $t = 5$ obtained using different incompressibility treatments; solid line: liquid-liquid interface from the reference Level-Set solution [30].

Fig. 12: The density mean value and the r.m.s. obtained for the lid-driven cavity flow at $Re = 1000$; the effect of: (a) the kernel choice, (b) $h/\Delta r$, (c) number of particles N influence in the WCSPH approach; (d) particles number N influence in both: ISPH-PPS and ISPH-GPPS techniques.

Fig. 13: The lid-driven cavity flow: density field at the steady-state solution.

Fig. 14: The density mean value and the r.m.s. obtained for the Rayleigh-Taylor instability (only upper phase $\varrho_U = 1.8\varrho_0$) using WCSPH and both ISPH approaches.

Fig. 15: The density field with local disturbance; left: the initial state (regular set of particles with one particle displaced), right: after 50 correction iterations.

Fig. 16: The lid-driven cavity velocity profiles at the steady-state against Ghia et al. [27] reference data ($Re = 1000$); results obtained using ISPH with PPS and Pozorski & Wawreńczuk correction [7] for the Wendland kernel [10], $h/\Delta r = 2$ and different number of particles N .

Fig. 17: The density mean value and r.m.s. obtained using the ISPH approach with PPS and Pozorski & Wawreńczuk density correction [7]; (a) the lid driven cavity ($Re = 1000$), (b) the Rayleigh-Taylor instability ($Re = 420$); the results obtained for the Wendland kernel [10] and $h/\Delta r = 2$.

Fig. 18: Histograms of the distance between the nearest pairs of the particles; the results obtained for the ISPH-PPS approach (a) without and (b) with the Pozorski and Wawreńczuk correction procedure.

Fig. 19: The Rayleigh-Taylor instability ($Re = 420$) computed using ISPH with PPS and Pozorski & Wawreńczuk density correction [7]; the black lines denote the interface position obtained by Grenier et al. [30] using the Level-Set formulation (312×624 cells).